Photoionization of Ar XVI and Ar XVII

Sultana N. Nahar *

Department of Astronomy, The Ohio State University, Columbus, OH 43210, USA

ABSTRACT

Photoionization of Li-like argon, $(h\nu + \text{Ar XVI} \rightarrow \text{Ar XVII} + e)$, and He-like argon, $(h\nu + \text{Ar XVII} \rightarrow \text{Ar XVIII} + e)$, are studied using the relativistic Breit–Pauli R-matrix (BPRM) method. Results include both the partial and total photoionization cross-sections of fine structure levels with $1/2 \leq J \leq 17/2$, $n \leq 10$ and $0 \leq l \leq 9$ of Ar XVI and with $0 \leq J \leq 10$, $n \leq 10$ and $0 \leq l \leq 9$ of Ar XVII. They correspond to 98 bound levels of Ar XVI and 191 of Ar XVII. The close coupling wave function expansion for Ar XVI included 17 core levels up to $n=3$ thresholds and that of Ar XVII 16 core levels up to $n=4$ thresholds. Because of high-lying core excitations of these ions, the photoionization cross-section, $\sigma_{PI}(nSLJ)$, decreases monotonically without features until at high energies where narrow high-peak resonances of Rydberg series of autoionizing states belonging to excited $n=2$ thresholds begin to appear. The dominant photoexcitation-of-core (PEC) or Seaton resonances also appear in the excited level cross-sections. The background of the total cross-section shows enhancement at $n=2$ thresholds due to resonant 1s–2p core excitations. However, the resonances become much weaker beyond $n=2$ thresholds. Radiation damping of resonances, important for these highly charged He- and Li-like ions, is included. These cross-sections are much improved over the existing TOPbase cross-sections where resonances, and background enhancements for Ar XVII were not included. With consideration of these effects, the present results should be accurate up to 10%–30% for various applications in modeling, recombination rates, opacities and diagnostic spectral analysis in the ultraviolet and X-ray regions. Cross-sections for H-like Ar are also included for completeness.

1. Introduction

Photoionization of highly charged ions, like the present He- and Li-like ions, can introduce absorption lines. These lines are commonly seen in the ultraviolet and X-ray regions of astrophysical spectra and are of great importance as they provide useful diagnostics for the plasmas. These lines are also used for fusion plasma diagnostics. Helium-like Ar lines have been measured in Seyfert galaxy NGC 3783 by Chandra space observatory (e.g. [1]).

Determination of ionization fractions, opacities, abundances, etc., require photoionization cross section. Earlier calculations for photoionization cross-sections for the argon ions, Ar XVI and Ar XVII, were carried out under the Opacity Project [2]. Peach et al. [3] studied Li-like ions using a 1 state calculations and Fernley et al. [4] He-like ions using 3-state calculations and pseudo orbitals. They were computed in the non-relativistic LS coupling approximation and using wave functions smaller than the present ones. The atomic data for the ions are available at the OP database, TOPbase [5].

2. Theory

Photoionization occurs directly,

$$h\nu + X^{+} \rightarrow e + X^{++}, \qquad (1)$$

* Tel.: +1 614 292 1888; fax: +1 614 292 2928.
  E-mail address: nahar@astronomy.ohio-state.edu
  URL: http://www.astronomy.ohio-state.edu/~nahar

as well as through an intermediate doubly excited auto-ionization state

$$e+X^{++} \leftrightharpoons (X^+)^{**} \leftrightharpoons \begin{cases} (a) \; e+X^{++} \, (AI) \\ (b) \; h\nu + X^+ \, (DR) \end{cases}. \qquad (2)$$

An autoionizing state leads either to autoionization (AI) where the electron goes free or to dielectronic recombination (DR) by emission of a photon. The inverse of DR is photoionization. The autoionizing resonances are included through the core excitations in close coupling (CC) wave function expansion in which the atomic system is represented by a 'target' or the 'core' ion of N-electrons system interacting with the $(N+1)$th electron. The $(N+1)$th electron is bound or in the continuum depending on its negative or positive energy (E). The total wave function, Ψ_E, of the $(N+1)$ electrons system in a symmetry $SL\pi$ is represented by an expansion as

$$\Psi_E(e+ion) = A\sum_i \chi_i(ion)\theta_i + \sum_j c_j \Phi_j, \qquad (3)$$

where the target ion eigenfunction, χ_i, is coupled with the $(N+1)$th electron function, θ_i. The sum is over the ground and excited core states. The $(N+1)$th electron with kinetic energy k_i^2 is in a channel labeled as $S_iL_i\pi_ik_i^2\ell_i(SL\pi)$. In the second sum, the Φ_js are bound channel functions of the $(N+1)$-electrons system that account for short range correlation and the orthogonality between the continuum and the bound electron orbitals. The details of the R-matrix method in the CC approximation can be found in, e.g. [6–9].

The relativistic effects are included through Breit–Pauli approximation [9,10]. The Hamiltonian of the $(N+1)$-electrons system is described in the Breit–Pauli R-matrix (BPRM) method by

$$H_{N+1}^{BP} = \sum_{i=1}^{N+1} \left\{ -\nabla_i^2 - \frac{2Z}{r_i} + \sum_{j>i}^{N+1} \frac{2}{r_{ij}} \right\} + H_{N+1}^{mass} + H_{N+1}^{Dar} + H_{N+1}^{so}, \qquad (4)$$

where the additional terms are relativistic one-body correction terms, the mass correction, $H^{mass} = -(\alpha^2/4)\sum_i p_i^4$, Darwin, $H^{Dar} = (Z\alpha^2/4)\sum_i \nabla^2(1/r_i)$, and the spin–orbit interaction, $H^{so} = Z\alpha^2\sum_i(1/r_i^3)\mathbf{l}_i.\mathbf{s}_i$. BPRM includes these and part of two-body interaction terms, such as the ones without the momentum operators [11].

Substitution of $\Psi_E(e+ion)$ in the Schrodinger equation

$$H_{N+1}\Psi_E = E\Psi_E, \qquad (5)$$

introduces a set of coupled equations that are solved using the R-matrix approach. The set of $SL\pi$ is recoupled for $J\pi$ levels of $(e + ion)$ system which is followed by diagonalization of the Hamiltonian, $H_{N+1}^{BP}\Psi = E\Psi$. The solution is a continuum wave function, Ψ_F, for an electron with positive energies $(E > 0)$, or a bound state, Ψ_B, at a negative total energy $(E \leq 0)$. The complex resonant structures in photoionization result from channel couplings between continuum channels that are open $(k_i^2 > 0)$, and ones that are closed $(k_i^2 < 0)$, at electron energies k_i^2 corresponding to autoionizing states of the Rydberg series, $S_iL_iJ_i\pi_i\nu\ell$ where ν is the effective quantum number, converging to the target thresholds.

Transition matrix elements for photoionization, $\langle \Psi_B \| \mathbf{D} \| \Psi_F \rangle$ where $\mathbf{D} = \sum_i \mathbf{r}_i$ is the dipole operator and the sum is over the number of electrons, are obtained from the bound and continuum wave functions. The transition matrix element can be reduced to generalized line strength as

$$\mathbf{S} = |\langle \Psi_j \| \mathbf{D}_L \| \Psi_i \rangle|^2 = \left| \left\langle \psi_f \left| \sum_{j=1}^{N+1} r_j \right| \psi_i \right\rangle \right|^2, \qquad (6)$$

where Ψ_i and Ψ_f are the initial and final state wave functions. The photoionization cross-section (σ_{PI}) is proportional to the generalized line strength as,

$$\sigma_{PI} = \frac{4\pi^2}{3c} \frac{1}{g_i} \omega \mathbf{S}, \qquad (7)$$

where g_i is the statistical weight factor of the bound state and ω is the incident photon energy.

Radiation damping of the resonances is important for He- and the Li-like ions. The radiative decay rates (A_r) for transitions, $2p(^2P_{3/2,1/2}^o) \longrightarrow 1s(^2S_{1/2})$ in H-like core and $1s2p\,(^1P_1^o) \longrightarrow 1s^2\,(^1S_0)$ in He-like core are comparable to autoionization rates, typically $A_a \sim 10^{12}-10^{14}$ s^{-1}, causing autoionizing resonances to considerable radiation damping. All resonances, up to effective quantum number $\nu \leq 10$, have been damped. The radiation damping of resonances is considered through a scheme on fitting the dipole matrix of the autoionizing resonance for autoionization and radiative decay rates whereby the radiative decay part is extracted out [12–14].

3. Computation

For Li-like Ar XVI, a wave function expansion with 17 core fine structure levels from configurations $1s^2$, $1s2s$, $1s2p$, $1s3s$, $1s3p$, and $1s3d$, and for He-like Ar XVII, a wave function expansion with 16 core fine structure levels from configurations $1s$, $2s$, $2p$, $3s$, $3p$, $3d$, $4s$, $4p$, $4d$ and $4f$ were used. These core levels are given in Table 1. Although core excitations up to $n=3$ for Ar XVI and up to $n=4$ for A XVII are considered, excitations up to $n=3$ is sufficient. The orbital wave functions of the core or the target were obtained from configuration interaction atomic structure calculations using the later version [15] of code SUPER-STRUCTURE (SS) [16]. The later version of SS includes contributions of the two-body Breit interaction. These wave functions were optimized with a set of configurations and a set of Thomas–Fermi scaling parameters for the orbitals. The set of correlation configurations and values of the scaling parameters for the core orbitals of Ar XVI are given in Table 1. For a core with a single electron, such as Ar XVIII, accurate energies are obtained easily and hence correlation configurations are not necessary. The Thomas–Fermi parameter for the orbitals were taken to be unity. Both the calculated and observed (NIST) level energies are given in Table 1. It may be noted that current NIST energies for Ar XVII differ some in the decimal values. As seen in Table 1, the calculated energies are very close, within 0.1%, to the observed values compiled in the NIST (website: www.nist.gov). However, the

Table 1
Target levels in the eigenfunction expansions of Ar XVI and Ar XVII, their energies in Ry, calculated E_c and observed E_o (NIST compilation). The correlation configurations and values of the λ parameters of the orbitals are given below.

	Ar XVII			Ar XVIII		
	Level	E_o	E_c	Level	E_o	E_c
1	$1s^2\,^1S_0$	0.0	0.0	1	$1s^2S_{1/2}$	0.0	0.0
2	$1s2s\,^3S_1$	228.15016	228.38	2	$2p^2P^o_{1/2}$	243.882	243.96
3	$1s2p\,^3P^o_0$	229.5280	229.69	3	$2s^2S_{1/2}$	243.893	243.97
4	$1s2p\,^3P^o_1$	229.57457	229.74	4	$2p^2P^o_{3/2}$	244.235	244.31
5	$1s2s\,^1S_0$	229.64803	229.79	5	$3p^2P^o_{1/2}$	289.165	289.25
6	$1s2p\,^3P^o_2$	229.77758	229.96	6	$3s^2S_{1/2}$	289.169	289.25
7	$1s2p\,^1P^o_1$	230.75281	230.97	7	$3d^2D_{3/2}$	289.270	289.35
8	$1s3s\,^3S_1$	270.03870	270.24	8	$3p^2P^o_{3/2}$	289.270	289.35
9	$1s3p\,^3P^o_0$	270.41843	270.61	9	$3d^2D_{5/2}$	289.305	289.38
10	$1s3p\,^3P^o_1$	270.43267	270.63	10	$4p^2P^o_{1/2}$	305.000	305.08
11	$1s3s\,^1S_0$	270.43506	270.61	11	$4s^2S_{1/2}$	305.002	305.08
12	$1s3p\,^3P^o_2$	270.49292	270.69	12	$4d^2D_{3/2}$	305.044	305.12
13	$1s3d\,^3D_2$	270.70333	270.90	13	$4p^2P^o_{3/2}$	305.044	305.12
14	$1s3d\,^3D_1$	270.70343	270.90	14	$4f^2F^o_{5/2}$	305.059	305.14
15	$1s3d\,^1D_2$	270.73840	270.94	15	$4d^2D_{5/2}$	305.059	305.14
16	$1s3p\,^1P^o_1$	270.75706	270.96	16	$4f^2F^o_{7/2}$	305.066	305.15
17	$1s3d\,^3D_3$	270.95804	270.92				

Ar XVII : correlations—$2s^2$, $2p^2$, $3s^2$, $3p^2$, $3d^2$, $2s2p$, $2s3s$, $2s3p$, $2s3d$, $2s4s$, $2s4p$, $2p3s$, $2p3p$, $2p3d$, $2p4s$, $2p4p$
λ_{nl}—1.1(1s), 0.99(2s), 1.1(2p), 1(3s), 1(3p), 1(3d), 1(4s), 1(4p)

observed energies used in the calculations as they provide more accurate resonance positions.

For Ar XVI, the second term of the wave function in Eq. (3), which represents the bound state correlation functions, includes all possible $(N+1)$-particle configurations with orbital occupancies from 0 to a maximum number as given within parentheses of the orbitals $1s(0-2)$, $2s(0-2)$, $3s(0-2)$, $3p(0-2)$, $3d(0-2)$, $4s(0-1)$, $4p(0-1)$. The radial integrals for interacting electron partial wave expansion are specified for $0 \leq \ell \leq 9$, with a R-matrix basis set of 30 continuum functions. The R-matrix boundary was chosen to be large enough, 5 a_o, to accommodate the bound orbitals. Computations are carried out for all angular momenta, $0 \leq L \leq 11$, $1/2 \leq J \leq 17/2$.

For Ar XVII, the bound state correlation functions included all possible configurations from 0 to maximum orbital occupancies, as given within parentheses, $1s(0-2)$, $2s(0-2)$, $2p(0-2)$, $3s(0-2)$, $3p(0-2)$, $3d(0-1)$, $4s(0-2)$, $4p(0-2)$, $4d(0-1)$, $4f(0-1)$. The partial wave expansion included all orbitals $0 \leq \ell \leq 9$, with a R-matrix basis set of 30 continuum functions. The R-matrix boundary was chosen to be 4 a_o. Computations are carried out for all angular momenta, $0 \leq L \leq 11$, $0 \leq J \leq 10$.

Both the partial and the total photoionization cross-sections with consideration of radiation damping are obtained for all bound levels using the BPRM R-matrix codes [9,17,14]. The narrow resonances of photoionization were delineated at a very fine energy mesh. The program

PBPRAD [18] extends the total photoionization cross-sections in the high energy region by a 'tail' using a fitting formula, $\sigma^o_{PI}(E^o/E)^m$, where E^o is the last tabulated energy beyond the resonances and $-1 \geq m \geq -3$ [17]. $m = -3$ for Kramers fit at very high energies. The energy levels are obtained from STGB and are identified using the code PRCBPID [19].

4. Results and discussions

Photoionization cross-sections for Ar XVI (Ar XVI + $h\nu \rightarrow$ Ar XVII + e) and Ar XVII (Ar XVII + $h\nu \rightarrow$ Ar XVIII + e) for a large number of bound levels, $n \leq 10$, for the ions are presented. The sets include both the total and the partial photoionization cross-sections.

There are 98 levels of Ar XVI with $n \leq 10$, $0 \leq l \leq 9$, $0 \leq L \leq 11$, and total angular momentum $1/2 \leq J \leq 17/2$ [20], and 191 of Ar XVII with $n \leq 10$, $0 \leq l \leq 9$, $0 \leq L \leq 9$, and total angular momentum $0 \leq J \leq 10$. The earlier results [20] are for oscillator strengths for radiative transitions in the BPRM approximation and hence are consistent with the present results for photoionization. They are obtained using the same wave function expansion.

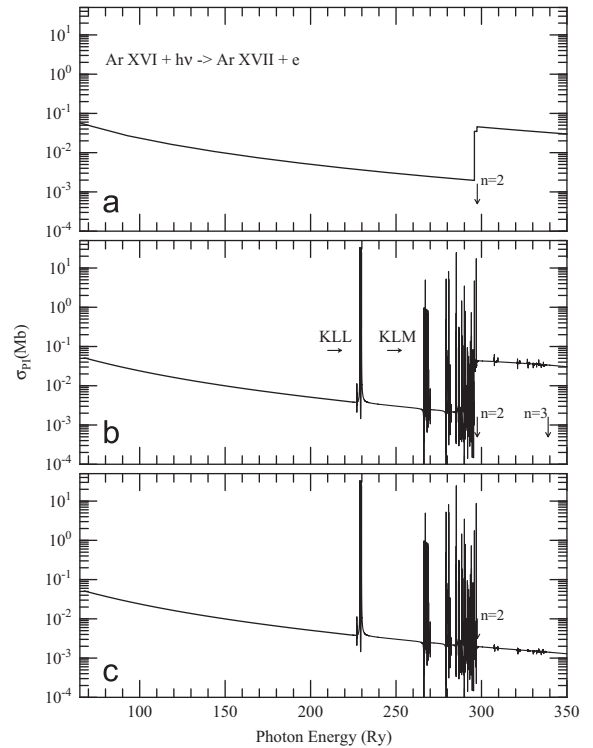The *total* photoionization cross-section (σ_{PI}) includes contributions from all channels for ionization in to ground

Fig. 1. Photoionization cross-sections σ_{PI} of the ground level $1s^22s$ ($^2S_{1/2}$) of Ar XVI: (a) total σ_{PI} from the TOPbase [3], (b) total σ_{PI} from present BPRM calculations, and (c) partial σ_{PI} from BPRM calculations. The earlier cross-sections did not include the resonances. The large enhancement in the total σ_{PI} around $n=2$ thresholds (~ 297 Ry) is due to core excitation ($h\nu + 1s^22p \rightarrow 1s2p + e$). No jump is in partial σ_{PI} as it includes only channels for ionization in to the ground level of core ion.

and various excited states of the residual ion, and *partial* cross-sections for ionization in to the ground state include contributions of the ground channel of the core only. Important characteristics in σ_{PI} are illustrated below.

Fig. 1 presents the photoionization cross-sections of the ground $1s^2\,2s\,^2S_{1/2}$ level of Ar XVI and compares with the existing total σ_{PI} obtained by Peach et al. [3] under the OP [2] and available at database TOPbase [5]. The earlier σ_{PI}, Fig. 1(a), did not include the strong and narrow resonances due to fine structure couplings as obtained in the BPRM approximation presented in panel (b). These resonances correspond to various Rydberg series $1snl\nu l'$ of autoionizing levels converging on to the $n=2$, 3 levels of the core ion. ν is the effective quantum number of an autoionizing state. The first resonance complexes are the well known KLL, KLM, etc. complexes belonging to $n=2$ core thresholds. KLL denotes the series $1s2l2l$, KLM denotes $1s2l3l'$, etc. The rise in the background at about 297 Ry (core excitation energy ~ 230 Ry plus the ionization energy of about 67 Ry) is due to $1s$–$2p$ excitation of the core during ionization. This inner-shell excitation threshold plays an important role in X-ray photoionization models.

Panel (c) of Fig. 1 presents partial σ_{PI} for photoionization leaving the core in the ground level. It can be noted that the total and partial cross-sections are identical below the first excited level, $n=2$ threshold, of the residual ion. However, these cross-sections do not show

the rise in the background since no channels for leaving the core in excited levels are included. These cross-sections are needed for applications such as for recombination cross-sections. The figure shows that the dominant resonances are due to series belonging to $n=2$ core levels beyond which the resonances become weaker.

PEC (photo-excitation-of-core) or the Seaton resonances [21] are very prominent in photoionization of excited levels of Ar XVI. Fig. 2 presents total σ_{PI} of excited Rydberg series of levels $1s^2 np(^2P^o_{1/2})$, $2 \le n \le 4$ of Ar XVI illustrating Seaton resonances at higher energies. These resonances are manifested by dipole transitions in the core ion and appear at the excited thresholds of transitions. At photon energies that equal to core excitation energies, the core goes through the allowed $\Delta J = 0-1$ transitions while the outer electron remains a 'spectator' in a doubly excited resonant state. The state decays via autoionization in to the ground level of the core. For Ar XVI, dipole transitions from core $1s^2$ to $n=2$ thresholds $1s2p^3P^o_1,{}^1P^o_1$ and $n=3$ thresholds $1s3p^3P^o_1,{}^1P^o_1$ occur at about 230 Ry and 270 Ry respectively. Hence the Seaton resonances appear at these energies as photons are absorbed (shown by arrows in Fig. 2). These resonances are more prominent than the narrow Rydberg resonances. Contrary to hydrogenic decay of the excited state cross-sections, Seaton resonances enhance the background. The partial cross-sections of excited levels of Ar XVI also show Seaton resonances due to core excitation.
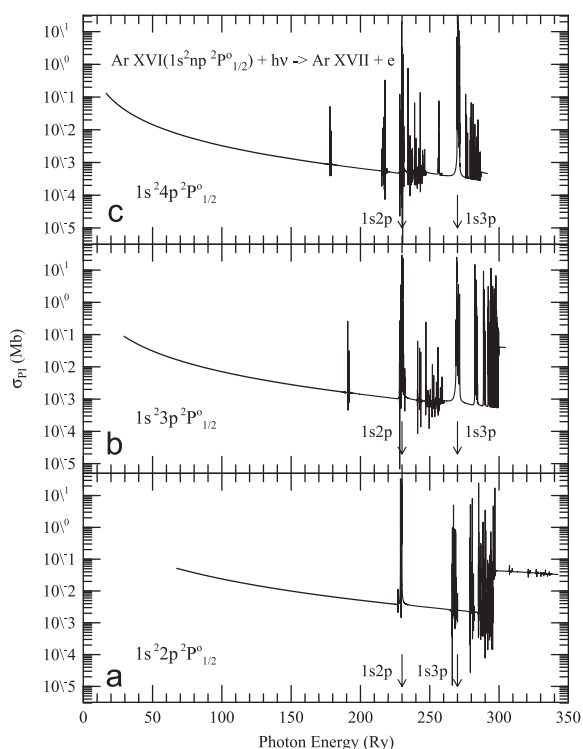

Fig. 2. Total photoionization cross-sections of the excited Rydberg series of levels, $1s^2 np(^2P^o_{1/2})$ with $2 \le n \le 4$, of Ar XVI. Prominent Seaton resonances due to core excitation to $n=2$ levels $1s2p^3P^o_1,{}^1P^o_1$ at about 230 Ry and to $n=3$ levels $1s3p^3P^o_1,{}^1P^o_1$ at about 270 Ry are pointed by arrows.
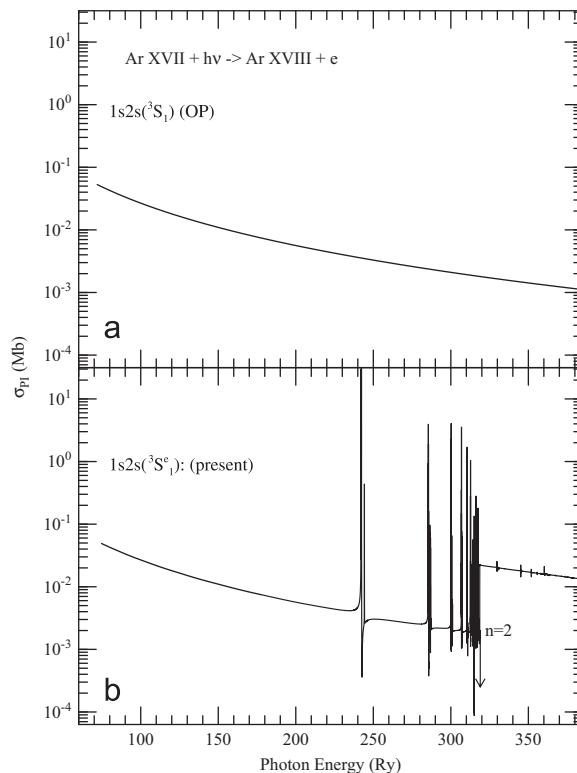

Fig. 3. Total σ_{PI} of $1s2s(^3S_1)$ state of Ar XVII: (a) by Fernley et al. 1987 [4] under the OP, (b) from BPRM calculations. The prominent high-peak resonances in (b) are due to Rydberg series of states belonging to core $n=2$ thresholds. The background enhancement is due to $1s$–$2p$ excitation of the core. Both effects are missing in the earlier σ_{PI}.

However, the partial cross-sections have lower background cross-sections.

Similar to Ar XVI, earlier photoionization cross-sections for He-like Ar XVII [4] under the OP [2] do not include the resonances. Fig. 3 compares photoionization cross-sections between earlier OP calculations [4] and the present BPRM calculations. The high-peak resonances in Fig. 3(b) correspond to Rydberg series belonging to $n=2$ thresholds of core Ar XVIII. The background enhancement is due to $1s–2p$ excitation of the core. It occurs during photoionization with core excitation $1s^2\,{}^2S_{1/2}-2p^2P^o_{1/2,3/2}$

$$h\nu + 1s(^2S_{1/2})2s^3S_1 \longrightarrow e + 2p^2P^o_{1/2,3/2}.$$
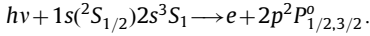
Both effects are missing in the earlier σ_{PI}.

Fig. 4 presents total photoionization cross-sections of five levels of Ar XVII: the top panel presents the ground level $1s^2$ ($^1S_0$) while the lower four panels show the illustrative features of the total σ_{PI} of four lowest $n=2$ excited levels that correspond to the prominent X-ray diagnostic lines in the Kα complex: (b) resonant line (w : $1s^2$ ($^1S_0$) ← $1s2p(^1P^o_1)$), (c) forbidden line (x : $1s^2$ ($^1S_0$) ← $1s2p(^3P^o_2)$), (d) intercombination line (y : $1s^2$ ($^1S_0$) ← $1s2p$ ($^3P^o_1$)), and (e) forbidden line (z : $1s^2$ ($^1S_0$) ← $1s2s(^3S_1)$), respectively. These four lines are seen resolved and prominent and hence most commonly used in spectral diagnostics for temperature, density, ionization balance, and abundances in plasma sources. Similar to Ar XVI, the core excited levels of Ar XVII lie at higher energy. Hence σ_{PI} does not show the Rydberg series of resonances until at high energy and decays smoothly at lower energy. The resonances in σ_{PI} are due to various Rydberg series $2l\nu l'$ of autoionizing levels converging on to the $n=2$, 3 levels of the core ion. The first resonance complexes are the well known LL, LM, etc. complexes belonging to $n=2$ core thresholds. LL denotes the series 2l2l, LM denotes 2l3l', etc. The enhancement at the excited $n=2$ thresholds at about 318 Ry (2p excitation energy ~ 244 Ry plus ionization energy ~ 74 Ry) is due to $1s–2p$ excitation as mentioned above. However, unlike Ar XVI, there is no sudden rise for the ground level since there is no $1s–2p$ excitation.

The excited levels of Ar XVII also exhibit Seaton resonances at photon energies for dipole transition in the core. The partial cross-sections for Ar XVII also show Seaton resonances due to core excitation. However, the partial cross-sections have lower background cross-sections and also contain less resonances as they correspond to less channels.

For completeness, photoionization cross-sections of H-like Ar XVIII have also been obtained. Fig. 5 presents photoionization cross-sections of five levels, ns(^2S), with $1 \leq n \leq 5$.

For both ions, Ar XVI and Ar XVII, the most dominating resonances belong to $n=2$ core levels. PEC or the Seaton resonances remain strong for $n=3$ excitations for many levels. Some improvement in photoionization cross-sections
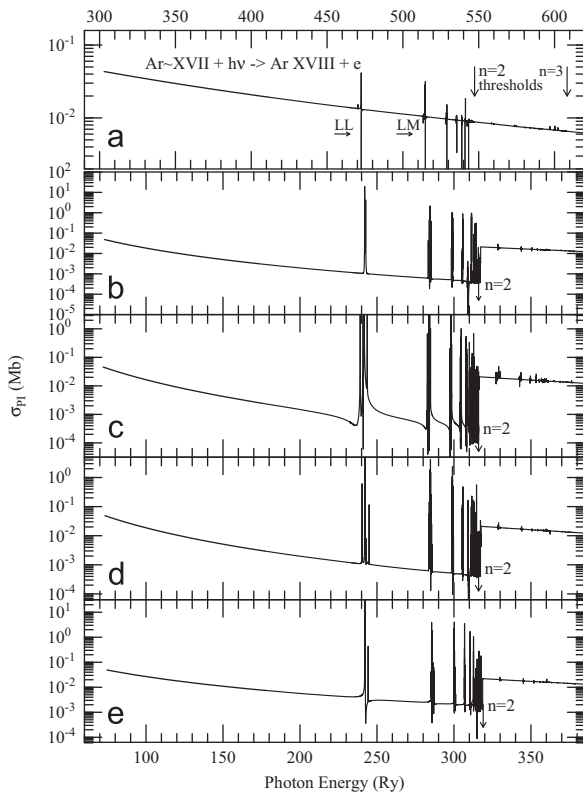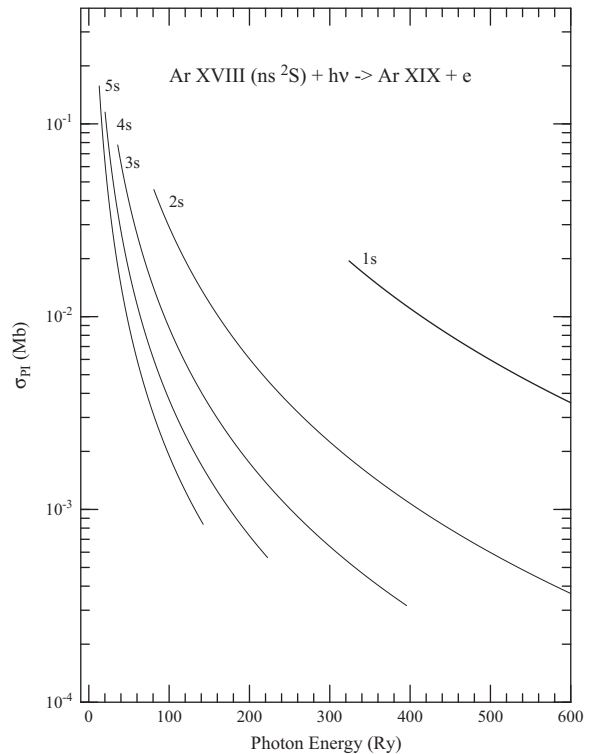

Fig. 4. Level-specific photoionization cross-sections of Ar XVII: (a) the ground level, $1s^2$ ($^1S_0$), and four excited (b) $1s2p(^1P^o_1)$, (c) $1s2p(^3P^o_2)$, (d) $1s2p(^3P^o_1)$, (e) $1s2s(^3S_1)$ levels corresponding to the prominent resonance (w), intercombination (y), and forbidden (x, z) diagnostic X-ray lines. A rise at $n=2$ threshold at about 318 Ry in the background σ_{PI} is noticed due to $1s–2p$ excitation in the core. The ground level does not have the rise.

Fig. 5. Photoionization cross-sections of 5 levels of Ar XVIII, ns(^2S), with $1 \leq n \leq 5$.

of Ar XVI could have been made by including the resonances belonging to core excitation of $n=4$ levels, as in the case for Ar XVII. One reason for not including $n=4$ core excitations is that, as seen for other few electron atomic systems and in the preliminary data for total recombination rates with respect to photoelectron energy for Ar XVI, which is the content of the next paper, the resonant contribution beyond $n=2$ levels decreases considerably. For Ar XVI, the total contribution from $n=3$ levels to recombination is over an order of magnitude lower than that from $n=2$ levels.

There can be some uncertainty in the background cross-sections of Ar XVI beyond $n=3$ thresholds due to missing K-edge rise. The background cross-section at various ionization edges of shells usually shows a rise which is typically smoothed out by resonances for complex ions. However, the rise can be seen when resonances are weaker. For Ar XVI, the rise for K-edge can be seen at $n=2$ thresholds for $1s^22p$ and $1s^23p$ levels (Fig. 2a, b), but not for $1s^24p$ level (Fig. 2c). It may be assumed that the K-edge ionization of an excited level $1s^2nl$ of a Li-like ion lies at threshold $1snl$. This implies that the wave function expansion should include the core threshold $1snl$ to see the K-edge rise of level $1s^2nl$. For the present calculations n goes up to 3. Although this rise diminishes with higher excited levels, the background cross-section could be underestimated for a number of excited levels.

5. Conclusion

Extensive sets of level-specific photoionization cross-sections, both partial and total, for Li-like Ar XVI and He-like Ar-XVII, obtained from relativistic BPRM method are presented. Large number of excited levels up to $n \leq 10$ for both the ions have been considered. Although the cross-sections of these ions show hydrogenic behavior in the low energy region, high-peak strong Rydberg and Seaton resonances exist in the higher energy region. These resonances correspond to various diagnostic complexes. It is important to incorporate these resonances for both photoionization and recombination rates of plasmas as these will show enhancement in the high energy and high temperature regions. The present cross-sections will be used for recombination cross-sections, rate coefficients, and diagnostics dielectronic satellite lines.

The present cross-sections are expected to be of high accuracy of about 10%–30% based on (i) inclusion of relativistic and (ii) radiation damping effects.

All photoionization data are available electronically from NORAD-Atomic-Data (NaharOSURadiativeAtomic-Data) website: www.astronomy.ohio-state.edu/nahar/nahar_radiativeatomicdata.

References

[1] Kaspi S, et al. Discovery of narrow X-ray absorption lines from NGC 3783 with the chandra high energy transmission grating spectrometer. Astrophys J 2000;535:L17–20.
[2] The Opacity Project Team. The opacity project, vol. 1, 1995, vol. 2, 1996, Institute of Physics Publishing.
[3] Peach G, Saraph HE, Seaton MJ. Atomic data for opacity calculations. IX. The lithium isoelectronic sequence. J Phys B 1988;21:3669–84.
[4] Fernley JA, Taylor KT, Seaton MJ. 6457 Atomic data for opacity calculations. VII. Energy levels, f values and photoionisation cross sections for He-like ions. J Phys B 1987;20:6457–76.
[5] The atomic data of the OP is available at TOPbase at ⟨http://cdsweb.u-strasbg.fr/topbase/topbase.html⟩.
[6] Burke PG, Robb WD. R-matrix theory of atomic processes. Adv Atomic Mol Phys 1975;11:143–214.
[7] Seaton MJ. Atomic data for opacity calculations. I. General description. J Phys B 1987;20:6363–78.
[8] Berrington KA, Burke PG, Butler K, Seaton MJ, Storey PJ, Taylor KT, et al. Atomic data for opacity calculations. II. Computational methods. J Phys B 1987;20:6379–97.
[9] Berrington KA, Eissner W, Norrington PH. RMATRIX1: Belfast atomic R-matrix codes. Comput Phys Commun 1995;92:290–420.
[10] Hummer DG, Berrington KA, Eissner W, Pradhan AK, Saraph HE, Tully JA. Atomic data from the IRON Project. 1: goals and methods. Astron Astrophys 1003;279:298–309.
[11] Pradhan AL, Nahar SN. In: Atomic astrophysics and spectroscopy. Cambridge University Press; 2011.
[12] Sakimoto K, Terao M, Berrington KA. Effects of radiative decay on the bound–continuum transition of highly charged atomic ions. Phys Rev A 1990;42:291–5.
[13] Pradhan AK, Zhang HL. Radiation damping of autoionizing resonances. J Phys B 1997;30:L571–9.
[14] Zhang HL, Nahar SN, Pradhan AK. Close coupling R-matrix calculations for electron-ion recombination cross sections. J Phys B 1999;32:1459–79.
[15] Nahar SN, Eissner W, Chen GX, Pradhan AK. Atomic data from the Iron Project—LIII. Relativistic allowed and forbidden transition probabilities for Fe XVII. Astron Astrophys 2003;408:789–801.
[16] Eissner W, Jones M, Nussbaumer H. Techniques for the calculation of atomic structures and radiative data including relativistic corrections. Comput Phys Commun 1974;8:270–306.
[17] Nahar SN, Pradhan AK. Unified treatment of electron-ion recombination in the close-coupling approximation. Phys Rev A 1994;49:1816–35.
[18] Nahar SN. Atomic data from the Iron Project LXII. Allowed and forbidden transitions in Fe XVIII in Breit–Pauli approximation. Astron Astrophys 2006;457:721–8.
[19] Nahar SN, Pradhan AK. Large-scale Breit–Pauli R-matrix calculations for transition probabilities of Fe V. Phys Scr 2000;61:675–89.
[20] Nahar SN. Relativistic fine structure oscillator strengths for Li-like ions: C IV—Si XII, S XIV, Ar XVI, Ca XVIII, Ti XX, Cr XXII, and Ni XXVI. Astron Astrophys 2003;389:716–28.
[21] Yu Y, Seaton MJ. Atomic data for opacity calculations. IV. Photoionisation cross sections for C II. J Phys B 1987;20:6409–29.